Evolving outer heliosphere: Large-scale stability and time variations observed by the Interstellar Boundary Explorer

D. J. McComas,[1,2] M. Bzowski,[3] P. Frisch,[4] G. B. Crew,[5] M. A. Dayeh,[1] R. DeMajistre,[6] H. O. Funsten,[7] S. A. Fuselier,[8] M. Gruntman,[9] P. Janzen,[10] M. A. Kubiak,[3] G. Livadiotis,[1] E. Möbius,[11] D. B. Reisenfeld,[10] and N. A. Schwadron[1,11]

Received 19 April 2010; revised 1 July 2010; accepted 2 September 2010; published 29 September 2010.

[1] The first all-sky maps of Energetic Neutral Atoms (ENAs) from the Interstellar Boundary Explorer (IBEX) exhibited smoothly varying, globally distributed flux and a narrow "ribbon" of enhanced ENA emissions. In this study we compare the second set of sky maps to the first in order to assess the possibility of temporal changes over the 6 months between views of each portion of the sky. While the large-scale structure is generally stable between the two sets of maps, there are some remarkable changes that show that the heliosphere is also evolving over this short timescale. In particular, we find that (1) the overall ENA emissions coming from the outer heliosphere appear to be slightly lower in the second set of maps compared to the first, (2) both the north and south poles have significantly lower (~10–15%) ENA emissions in the second set of maps compared to the first across the energy range from 0.5 to 6 keV, and (3) the "knot" in the northern portion of the ribbon in the first maps is less bright and appears to have spread and/or dissipated by the time the second set was acquired. Finally, the spatial distribution of fluxes in the southernmost portion of the ribbon has evolved slightly, perhaps moving as much as 6° (one map pixel) equatorward on average. The observed large-scale stability and these systematic changes at smaller spatial scales provide important new information about the outer heliosphere and its global interaction with the galaxy and help inform possible mechanisms for producing the IBEX ribbon.

Citation: McComas, D. J., et al. (2010), Evolving outer heliosphere: Large-scale stability and time variations observed by the Interstellar Boundary Explorer, *J. Geophys. Res.*, *115*, A09113, doi:10.1029/2010JA015569.

1. Introduction

[2] The Interstellar Boundary Explorer (IBEX) mission (see *McComas et al.* [2009a] and other papers in the IBEX Special Issue of Space Science Reviews) recently provided the first global observations of the heliosphere's interstellar interaction. These observations included energy-resolved, all-sky images of energetic neutral atoms (ENAs) over the energy range from ~0.1–6 keV, emanating from the outer heliosphere [*McComas et al.*, 2009b; *Fuselier et al.*, 2009; *Funsten et al.*, 2009a; *Schwadron et al.*, 2009]. Generally speaking, while some aspects of IBEX ENA observations were consistent with prior expectations, many were not. In particular, IBEX discovered a narrow "ribbon" of significantly enhanced ENA emissions passing between the directions of the two Voyager spacecraft in the sky. Additional observations at higher energies from the Cassini spacecraft [*Krimigis et al.*, 2009] indicate a broader band of enhanced emissions that generally lies close to the IBEX ribbon near the equator and in the northern hemisphere, but deviates significantly from the ribbon in the south. Finally, the first direct measurements of interstellar neutral H and O were also made by IBEX [*Möbius et al.*, 2009]. In this study, we provide new ENA observations from IBEX, covering its complete second set of sky maps, and focus on determining if and how these maps (and the outer heliosphere itself) may be evolving over short (half year) timescales.

[3] The narrow ribbon discovered by IBEX is superposed on a globally distributed ENA flux that is organized by

[1]Southwest Research Institute, San Antonio, Texas, USA.
[2]Department of Physics and Astronomy, University of Texas at San Antonio, San Antonio, Texas, USA.
[3]Space Research Centre, Polish Academy of Sciences, Warsaw, Poland.
[4]Department of Astronomy and Astrophysics, University of Chicago, Chicago, Illinois, USA.
[5]Kavli Institute for Astrophysics and Space Research, Massachusetts Institute of Technology, Cambridge, Massachusetts, USA.
[6]Applied Physics Laboratory, Johns Hopkins University, Laurel, Maryland, USA.
[7]Los Alamos National Laboratory, Los Alamos, New Mexico, USA.
[8]Lockheed Martin Advanced Technology Center, Palo Alto, California, USA.
[9]Division of Astronautical Engineering, Viterbi School of Engineering, University of Southern California, Los Angeles, California, USA.
[10]Department of Physics and Astronomy, University of Montana, Missoula, Montana, USA.
[11]Space Science Center, University of New Hampshire, Durham, New Hampshire, USA.

0148-0227/10/2010JA015569

ecliptic latitude and longitude (essentially solar latitude and the direction of motion with respect to the local interstellar medium, LISM) [*McComas et al.*, 2009b; *Fuselier et al.*, 2009; *Funsten et al.*, 2009a; *Schwadron et al.*, 2009]. ENA fluxes in the ribbon reach maxima ~2–3 times higher than the surrounding regions, and while the ribbon is variable in width from <15° to >25° full width at half maximum (FWHM) along its length [*McComas et al.*, 2009b; *Fuselier et al.*, 2009], it averages ~20° wide over a broad energy range of IBEX's energy steps centered on energies from 0.7 to 2.7 keV [*Fuselier et al.*, 2009]; this analysis did not remove the intrinsic width of the IBEX sensors' angular response (~7°FWHM), so the real average width of the ribbon is actually thinner <20°. Even more remarkably, the ribbon also shows statistically significant fine structure that is at most a few degrees across [*McComas et al.*, 2009b]. The center of the ribbon passes ~25° away from the upwind direction or "nose" of the heliosphere and has brighter emissions from somewhat broader regions at higher latitudes in both hemispheres, around ~60°N and ~40°S ecliptic latitudes [*McComas et al.*, 2009b; *Funsten et al.*, 2009a]. The northern bright region or "knot" has a different spectral shape than the rest of the ribbon with an enhancement (bump) at higher energies, consistent with the shape of other near-pole energy spectra [*Funsten et al.*, 2009a]. In fact, the ribbon has nearly the same average spectral slope and shape as surrounding regions at all heliolatitudes [*McComas et al.*, 2009b; *Funsten et al.*, 2009a].

[4] One of IBEX's remarkable discoveries about the ribbon is that it appears to be ordered by the most likely direction of the interstellar magnetic field just outside the heliopause (**B**), and in particular seems to lie where **B** is nearly perpendicular to IBEX's radially directed (**r**) line of sight (LOS), which is where $\mathbf{B} \cdot \mathbf{r} = 0$ [*McComas et al.*, 2009b; *Schwadron et al.*, 2009]. This direction is based on inferred flow deflections between interstellar H and He [*Lallement et al.*, 2005], which are also consistent with the direction inferred from 2 to 3 kHz radio emissions measured by the Voyager spacecraft [*Gurnett et al.*, 2006]. The model of the draped, local magnetic field [*Pogorelov et al.*, 2009] that very closely matches the IBEX ribbon [*Schwadron et al.*, 2009] incorporates these flow deflections, the observed ~10 AU difference between the termination shock (TS) crossing distances of Voyagers 1 and 2 [*Stone et al.*, 2008], and the inferred interstellar densities just outside the heliosphere [*Slavin and Frisch*, 2008; *Bzowski et al.*, 2008].

[5] The ribbon weakens, but continues to extend around the north ecliptic pole, nearly closing a loop on the sky [*McComas et al.*, 2009b; *Funsten et al.*, 2009a; *Schwadron et al.*, 2009]. The "center" of this loop in the first set of IBEX sky maps is at ~39° ecliptic latitude and ~221° ecliptic longitude [*Funsten et al.*, 2009a]. Ultimately, the combination of simulations of detailed draping and compression of the interstellar field [e.g., *Pogorelov et al.*, 2009; *Schwadron et al.*, 2009, and references therein] with multiple sets of all-sky maps from IBEX will likely provide the most accurate direction of the local interstellar magnetic field.

[6] The IBEX observations show the brightest regions of ribbon at mid- to high latitudes, where slow and fast solar winds interact in corotating interaction regions (CIRs). Thus, it seems likely that the ribbon emissions are at least partially related to the solar wind properties as well as to the external environment. Finally, as pointed out by *McComas et al.* [2009b], while the ribbon appears as a generally continuous region of emissions, it could easily be a string of localized and sometimes overlapping "knots" of emission. In fact, the fine structure in the ribbon suggests that whatever mechanism creates the ribbon emissions must be highly spatially variable.

[7] Various possible explanations for the source of the ribbon were identified by *McComas et al.* [2009b], with additional analysis on several of these provided by *Fuselier et al.* [2009], *Funsten et al.* [2009a], and *Schwadron et al.* [2009]. These explanations spanned possibilities of how the ribbon emissions might be generated in the inner heliosheath (between the TS and heliopause), in the solar wind (inside the TS), and in the outer heliosheath (beyond the heliopause). The six possible sources of the IBEX ribbon identified and briefly discussed by *McComas et al.* [2009b] are summarized schematically in Figure 1 and described below.

1.1. Maximum Pressure and Stagnation (1 in Figure 1)

[8] The first general area of possible explanations centers on the observations of enhanced particle pressure within the ribbon [*McComas et al.*, 2009b; *Funsten et al.*, 2009a; *Schwadron et al.*, 2009]. This enhanced pressure could be generally balanced by enhanced external pressure from the combination of the external plasma dynamic and magnetic ($J \times B$) forces, producing a localized band of maximum total pressure around the heliopause. Such enhanced pressure at the heliopause might propagate throughout the inner heliosheath, adjusting the plasma properties and bulk flow in such a way that the ribbon might indicate the true region of highest pressure in the inner heliosheath. If so, the flow would stagnate in this region and ion densities and ENA emissions would be enhanced. As pointed out by *McComas et al.* [2009b], if the ribbon does represent the region of highest pressure, then it would divide flows through the inner heliosheath, analogous to a continental divide, which might explain the unusual flow directions observed at the locations of the two Voyager spacecraft in the inner heliosheath.

[9] An extension of this concept discussed by these authors was that the additional pressure might also extrude small regions of the heliopause forming limited outward bulges in the heliopause in the regions where the field was laying most tightly along its surface; such "herniations" might collect ions, producing very high densities and almost no bulk flow, potentially explaining the observed fine structure. This general explanation could naturally account for the fact that the ribbon has a very similar spectral slope and shape of the surrounding regions, as the enhanced ENA flux would arise naturally from the accumulation of particles already in the inner heliosheath. Simulations and observations appear to be at odds with one another concerning this mechanism. On the other hand, magnetohydrodynamic (MHD) simulations of the heliospheric interaction, including kappa distributions to emulate effects of enhanced tails of higher-energy pickup ions [*Prested et al.*, 2008; *Izmodenov et al.*, 2009; *Pogorelov et al.*, 2009], indicate maximum pressure in the inner heliosheath near the nose and not along an extended region significantly offset from the nose, such as the ribbon. Surely, the actual conditions in the inner heliosheath are more complicated than accounted for in the

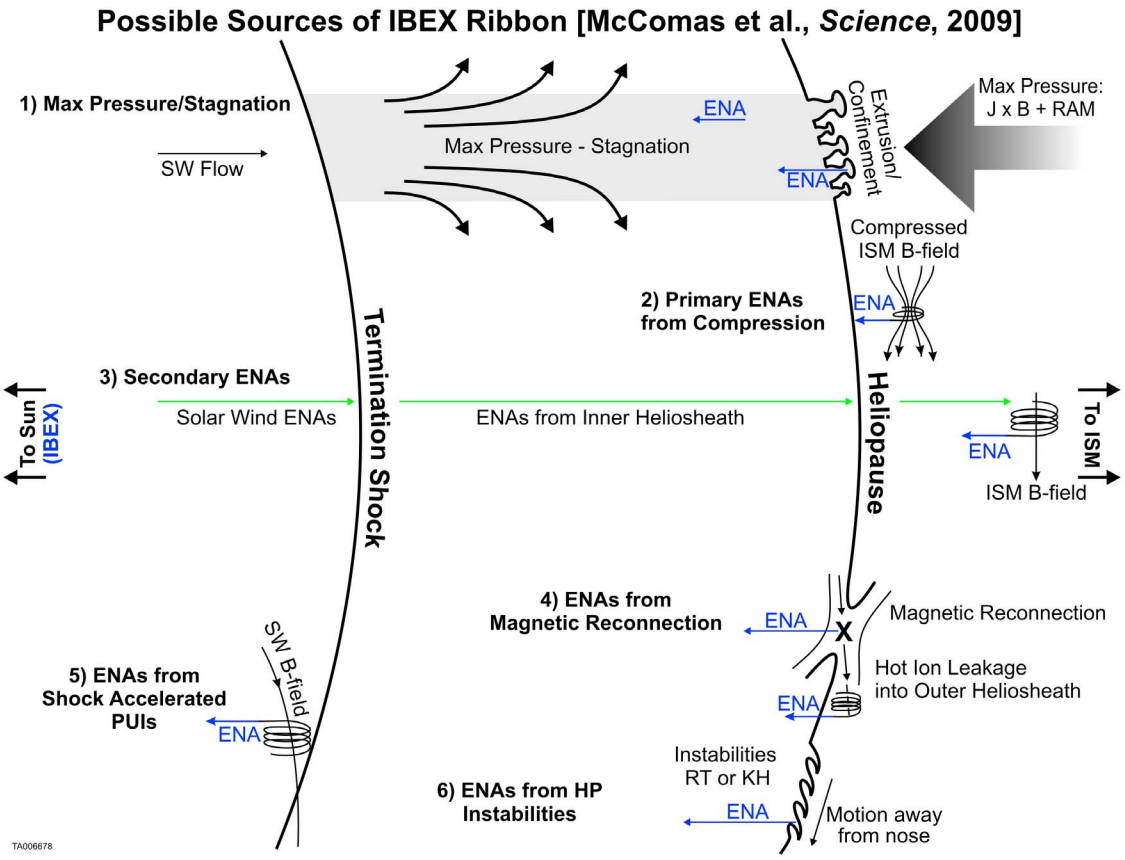

Figure 1. Schematic diagram summarizing the six possible sources of the ribbon of enhanced ENA emissions in the IBEX data identified by *McComas et al.* [2009b]. These comprise (1) ENAs produced in a region of maximum pressure and stagnation in the inner heliosheath, possibly producing extrusions of the heliopause; (2) ENAs preferentially produced with ~90° pitch angles through localized compression of the very local interstellar magnetic field outside the heliopause; (3) secondary ENAs produced by ionization and subsequent reemission of outward traveling ENAs from the solar wind and pickup ions inside the termination shock and/or from the inner heliosheath; (4) ENAs produced in association with magnetic reconnection across the heliopause; (5) ENAs produced from shock accelerated ions just upstream and downstream of the termination shock; and (6) ENAs produced in enhanced localized regions at the heliopause, owing to the development of Rayleigh-Taylor and/or Kelvin-Helmholtz instabilities.

current models, with (as initially suggested by *Zank et al.* [1996]) a much smaller (~20% by number) pickup ion population receiving the vast majority of the energization at the TS [*Richardson et al.*, 2008, 2009]. A start was made at more carefully addressing the role of the TS in processing the solar wind and pickup ions [*Zank et al.*, 2010], however much more theoretical work is needed in this area. Perhaps the complete treatment of this far more complicated plasma in future simulations will reduce the discrepancies between the simulations and observations.

1.2. Primary ENAs From Compression (2 in Figure 1)

[10] Another pair of related explanations (2 and 3 in Figure 1) invoke the possibility of ribbon emissions coming from outside the heliopause, from regions where the external $\mathbf{B} \cdot \mathbf{r} = 0$ [*McComas et al.*, 2009b; *Schwadron et al.*, 2009] (see above). Compression of the external field would increase densities and provide perpendicular heating, producing more perpendicular pitch angle distributions (enhanced particles around 90° pitch angles) where they would preferentially emit in a plane that includes the inward radial direction. Thus, local compressions in the outer heliosheath magnetic field would preferentially emit ENAs that would be observable in the inner heliosphere by IBEX in exactly the regions where the average external field is most perpendicular to the radial LOS.

1.3. Secondary ENAs (3 in Figure 1)

[11] In addition to interstellar ions, the external magnetic field is populated with particles from ionization of outward traveling ENAs from both the solar wind region inside the TS and the inner heliosheath. This source is labeled "secondary ENAs" as they have been through the ion-to-ENA conversion process twice. These ions would have relatively perpendicular pitch angle distributions and be further compressed in regions where $\mathbf{B} \cdot \mathbf{r} = 0$. The primary problem with this process for producing the ribbon, as pointed out by *McComas et al.* [2009b], is that pitch angle distributions

would need to remain nearly perpendicular for times comparable to or longer than neutralization times in the outer heliosheath, times typically thought to be a few years. A simulation by *Izmodenov et al.* [2009] including the secondary ENA source assumed comparatively rapid isotropization and did not produce a ribbon-like structure. Since the publication of the IBEX results, however, two different 3-D MHD simulations [*Heerikhuisen et al.*, 2010; *Chalov et al.*, 2010] have produced a structure very much like the overall ribbon structure by assuming that perpendicular pitch angle distributions can survive long enough for ions to reneutralize. If this assumption could somehow be validated, this secondary ENA process would be a highly viable explanation for producing the ribbon. Finally, generating observed fine structure in the ribbon with this process would further require bunched ENAs produced by initially bunched solar wind ions or pickup ions, or additional small-scale compressions of the magnetic field as discussed in section 1.2.

1.4. ENAs From Magnetic Reconnection at the Heliopause (4 in Figure 1)

[12] Another possible mechanism identified by *McComas et al.* [2009b] was that ribbon ENAs might result from magnetic reconnection across the heliopause. Reconnection would allow hot heliosheath ions to propagate out into cooler, denser outer heliosheath plasma. Magnetic reconnection could produce narrowly confined magnetic structures potentially consistent with both "knots" and fine structure observed in the ribbon. The external pressure is greatest along the ribbon [*Schwadron et al.*, 2009], which generally enhances the rate of magnetic reconnection. However, the magnetic field in the inner heliosheath is highly variable [*Burlaga et al.*, 2006], and the average field just inside of the heliopause is expected to be "painted" with narrow alternating bands of oppositely directed field [*Suess*, 2004], so it is not obvious why reconnection would be limited to a narrow structure like the ribbon.

1.5. ENAs From Shock-Accelerated Pickup Ions (5 in Figure 1)

[13] Yet another possible mechanism discussed by *McComas et al.* [2009b] was that the ribbon ENAs might be coming from the region around the TS, perhaps from shock-accelerated pickup ions [*Chalov and Fahr*, 1996; *Fahr et al.*, 2009] propagating inward through the region where the solar wind decelerates significantly (~20%) in the last ~10 AU just inside the TS [*Richardson et al.*, 2008]. Again, however, it is not obvious why this mechanism would produce a ribbon instead of broadly distributed regions of enhanced emissions.

1.6. ENAs From Heliopause Instabilities (6 in Figure 1)

[14] Finally, *McComas et al.* [2009b] suggested that large-scale, Rayleigh-Taylor and/or Kelvin-Helmholtz-like instabilities might confine hot, inner heliosheath plasma in narrow structures along the heliopause boundary. Such instabilities can be driven by neutrals destabilizing the boundary. Some models [e.g., *Borovikov et al.*, 2008] produce large (>10 AU), semicoherent structures with higher ion densities that move tailward at tens of km s^{-1} along the heliopause boundary.

[15] The various possible mechanisms are not mutually exclusive; in fact some combination or combinations may well ultimately explain the ribbon. One such example that is being actively pursued (H. Kucharek et al., manuscript in preparation, 2010) combines maximum pressure and stagnation and ENAs from shock-accelerated pickup ions. If a pressure maximum (1 in Figure 1) propagates through the inner heliosheath and indents the TS, ions that specularly reflect off the indented part of the TS (as part of the shock formation process) will have gyrovelocity vectors directed back toward the Sun (5 in Figure 1). ENAs produced by charge exchange of these ions may account for the ribbon and fine structure within it.

[16] While the basic mechanisms delineated above are under consideration for explaining the IBEX ribbon, none produces the full range of observations without making significant, unsubstantiated assumptions, and perhaps the ribbon arises from some completely different mechanism. In fact, a seventh possible mechanism has been suggested by *Grzedzielski et al.* [2010]. These authors propose a novel interpretation where the ribbon does not arise from the heliospheric interaction at all, but instead from ENAs produced by charge exchange between neutral H atoms at the nearby edge of the local interstellar cloud (LIC) and hot protons from the Local Bubble. They argue that for reasonable assumptions about local densities, such galactic ENAs should be able to reach the heliosphere provided that the edge is close enough (less then ~500–2000 AU).

[17] While IBEX data support some earlier ideas, in other areas a completely new paradigm is needed for understanding the interaction between our heliosphere and the galactic environment. This study examines the possibility of time evolution of the heliospheric interaction in general, and IBEX ribbon in particular, by comparing the first set of 6 month IBEX sky maps with the new set of maps generated over the subsequent 6 months of observations. Observations of temporal evolution in IBEX ENA measurements are pivotal for understanding this interaction in general and for testing the various hypotheses that may account for the unexpected structures, such as the ribbon.

2. Observations From IBEX

[18] IBEX is a spinning spacecraft with a spin rate of 4 RPM and spin axis (and solar array) pointed toward the Sun. Each orbit (orbital period ~7.5 days) around perigee, the spin axis is repointed back toward the Sun to compensate for the ~1°/d drift as the Earth orbits the Sun. Therefore, observations from each orbit provide ~7° wide "swaths," at multiple energies, that collectively produce a set of all-sky maps each 6 months. The full width at half maximum (FWHM) angular resolution of the IBEX ENA cameras is also ~7°, so, by design, the repointing and intrinsic angular resolution are roughly matched. In this study we show observations from the IBEX-Hi sensor for energy steps (or passbands) 2–6; Table 1 provides the nominal (peak) energy and energy range of each energy step [*Funsten et al.*, 2009b]. Detailed information about all aspects of the mission is available from *McComas et al.* [2009a] and other papers in the IBEX Special Issue of Space Science Reviews.

[19] Figure 2 schematically shows the geometry of the IBEX orbit over the year. The Earth's magnetosphere

Table 1. Energy Passbands for IBEX-Hi (Qualified Triple-Coincidence Detections)

E Step	E_{-FW} (keV)	E_{-FWHM} (keV)	$E_{Nominal}$ (keV)	E_{+FWHM} (keV)	E_{+FW} (keV)	$\Delta E/E$ FWHM (keV)
2	0.35	0.52	0.71	0.95	1.23	0.60
3	0.58	0.84	1.08	1.55	1.93	0.65
4	1.07	1.36	1.85	2.50	3.02	0.62
5	1.68	1.99	2.70	3.75	4.54	0.65
6	2.57	3.13	4.09	6.00	6.93	0.70

(shaded) is oriented away from the Sun, so different seasons have quite different magnetospheric backgrounds and obscuration. The first maps were made while IBEX's apogee was largely on the sunward side of Earth, where much of the time IBEX was outside the Earth's bow shock and in the solar wind. The second set of sky maps were produced from orbits as IBEX's apogee crossed through the magnetotail. Commissioning of the IBEX-Hi sensor [*Funsten et al.*, 2009b] was completed in Orbit 10, so the first sky maps were taken over Orbits 11–33 (25 December 2008 through 18 June 2009), while the second were from Orbits 34–56 (18 June through 10 December 2009).

[20] Figure 3 provides a comparison of the first (Figure 3, left) and second (Figure 3, right) sets of sky maps in the spacecraft frame of reference. From top to bottom, the maps show data in the top five energy channels of IBEX-Hi, labeled with the nominal central energies for each passband (see Table 1). For each energy step, maps are compared using a consistent color scale. While some corrections are required to make quantitative comparisons between maps at each energy, the uncorrected observations in Figure 3 clearly show generally similar ENA fluxes and the presence of the ribbon in roughly the same location for both the first and second maps.

[21] In order to quantitatively compare sky maps taken 6 months apart, we first consider processes that could affect the measured fluxes of ENAs at IBEX. These include (1) the finite probability of ionization of ENAs on their way into 1 AU from the outer heliosphere, (2) a very small energy change of ENAs due to the combined actions of solar gravity and radiation pressure, and (3) the finite speed of the proper motion of the IBEX detectors with respect to the Sun (the Compton-Getting effect). The first two of these effects can be significant at lower energies, but only have very minor influence on the ENAs in the energy ranges examined here (~0.5–6 keV). This is particularly true for quiet times of the Sun and the solar wind, in which both the ionization probability and radiation pressure are smallest. The past several years have been among the quietest times observed with the most prolonged, lowest power interval of solar wind since the start of the space age [*McComas et al.*, 2008]. While these two effects are at work at all distances along the trajectory of an ENA, they have the largest quantitative impact over the last ~10 AU as ENAs travel through the inner heliosphere approaching IBEX.

[22] For this study, we calculated the combined effects of ionization and gravity/solar wind pressure using recent solar observations from the Timed/SEE series (Lyman-alpha [*Woods et al.*, 2005]), SOLAR 2000 (photoionization rate [*Tobiska et al.*, 2000]), the OMNI-2 time series (charge exchange with solar wind particles [*King and Papitashvili*, 2005]), and a model of the solar wind and radiation pressure latitude anisotropy [*Bzowski*, 2008]. We carried out the calculations for both spherically symmetric and latitude-dependent solar wind structures following the approach proposed by *Bzowski* [2008], who took into account (apart from the primary effects mentioned above) secondary effects such as the Doppler dependence of the radiation pressure on the radial velocity of the atoms due to the self reversal of the solar Lyman-alpha line profile [*Tarnopolski and Bzowski*, 2009], ionization by solar wind electrons [*Bzowski et al.*, 2008], latitude variation of the Lyman-alpha intensity [*Auchère et al.*, 2005], and change of instantaneous charge-exchange rate due to the change in relative velocity between the incoming ENA and the expanding solar wind. The ecliptic 1 AU values of the relevant parameters are shown in Figure 4. While there are a variety of short-duration fluctuations in these parameters up to and including monthly (solar rotations) variations, the overall properties are very similar over the intervals covering the first two sets of IBEX maps. One notable exception is a solar wind event just before 2009.5, when a short, abrupt increase in solar wind density (by a factor of ~6) occurred, resulting in a similar brief increase in the charge-exchange rate.

[23] Our model solar parameters as a function of heliolatitude are based on observations obtained during the pre-

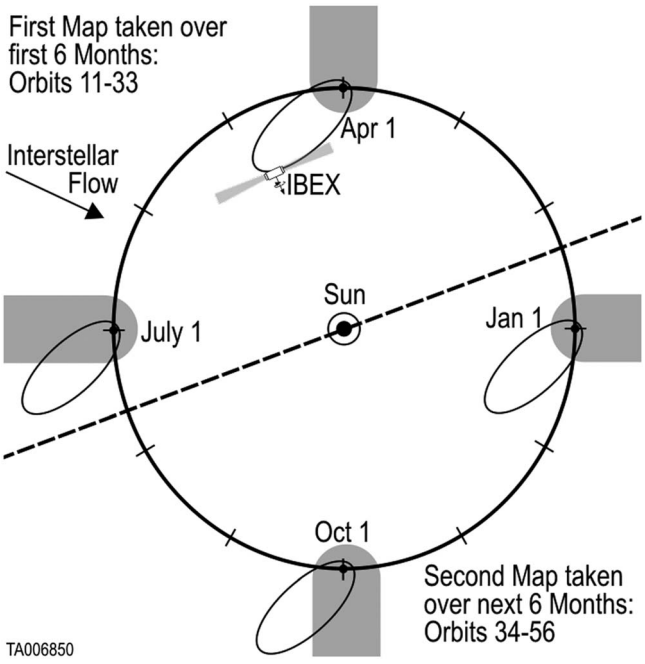

Figure 2. Schematic diagram of IBEX orbital geometry showing the inertially fixed IBEX orbit with respect to the Earth and magnetosphere (gray) over the year. The IBEX spacecraft is repointed once each orbit and views perpendicular to its Sun-pointing spin axis. The first and second maps were taken over separate halves of the Earth's orbit, with IBEX's apogee being mostly sunward of the Earth for the first maps and tailward for the second.

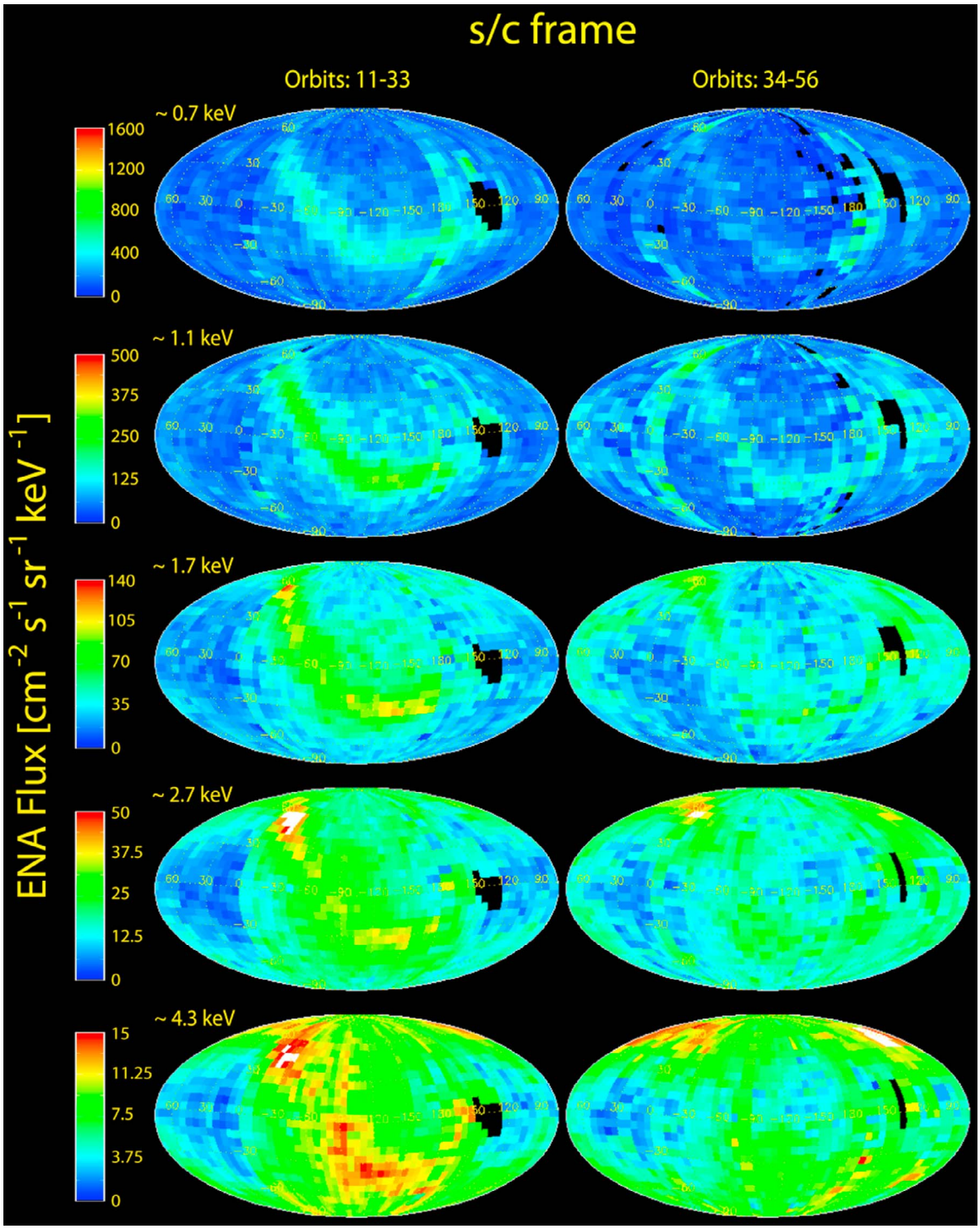

Figure 3. IBEX-Hi observations showing the (left) first and (right) second sets of all-sky maps in spacecraft coordinates. Both sets of maps show similar fluxes and the existence of the ribbon of enhanced emissions. The maps are shown in Mollweide projections with the nose of the heliosphere in the center of each map and the tail at both the far left and far right; angles are given in ecliptic J-2000 latitude and longitude.

vious solar cycle [*Bzowski et al.*, 2003; *Bzowski*, 2008]. Here we calculate survival probabilities of H ENAs using this 3-D model as well as validating the 3-D results by comparing with a simpler 2-D calculation where parameters do not depend on heliolatitude. We examined the survival probabilities of H ENAs for the times and geometry of IBEX observations used to construct the first two sets of IBEX maps for the central energies of IBEX-Hi energy steps 2 through 6. Small latitude variations in survival probability were obtained from the 3-D calculation for

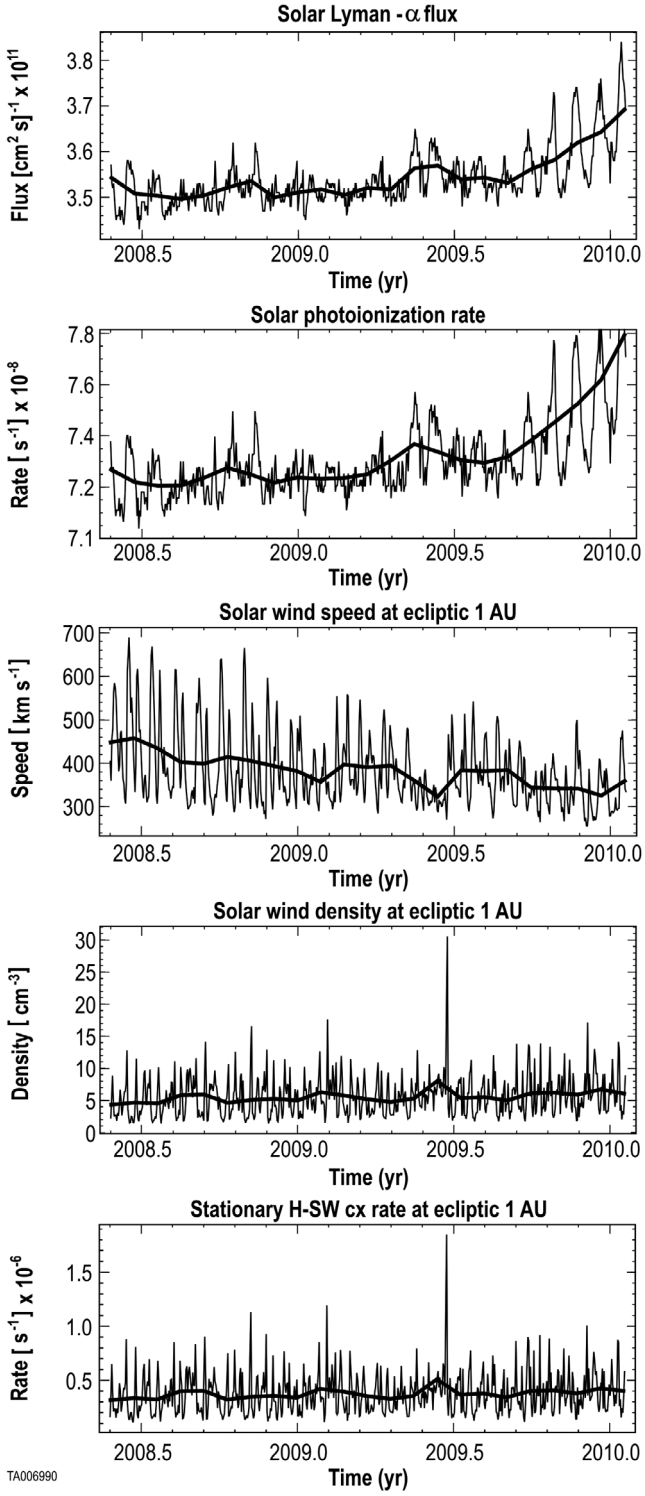

Figure 4. Daily (thin lines) and running 27 day averages (thick lines) of solar radiation and solar wind parameters relevant for calculating ionization rates of H ENAs observed by IBEX (see text).

ENAs approaching from higher latitudes. Overall, however, the amplitude of latitudinal modulation due to ionization (losses) of the ENAs in the supersonic solar wind are only a few percent and thus have little impact on the IBEX maps.

[24] We compared the survival probabilities for the time interval of the second set of IBEX maps and calculated differences between the probabilities for the first and second sets of maps. This comparison of survival probabilities shows that the effect on the survival probabilities of violent and abrupt, but short-timed, events in the solar wind, such as the event that happened shortly before 2009.5, is barely discernable. Figure 5 shows the results of the 3-D calculations where the ratio of survival probabilities is color coded as a function of spacecraft spin phase and orbit number (from the second set of maps); ratios for other energy steps are intermediate between the results shown here. The resulting difference in survival probabilities between the equivalent orbits do not exceed 15% and typically only ~5–10% for IBEX-Hi energy step 2 (the lowest one shown in this study). For the rest of the higher-energy steps, these ratios are even smaller.

[25] From our extensive calculations of these effects, we conclude that departures of differences between the two sky maps of more than ~10% are most likely due to real changes in the outer heliosphere and not modulation of ENAs propagating back through the solar wind. In this study we chose to leave these corrections out of the IBEX data being displayed in order to keep it as close as possible to the raw data and allow the reader to independently assess the veracity of the temporal changes observed. One note of caution for future studies of time variation is that the solar environment has been unusually quiet since the start of IBEX observations. As the Sun becomes more active and the solar wind more variable, these effects will become more significant and will require the IBEX team to make explicit compensation or correction.

[26] In contrast to the effects discussed above, we did need to make an explicit Compton-Getting (CG) correction in order to quantitatively compare the first and second sets of maps. This correction removes effects of the Earth's (and IBEX spacecraft's) ~30 km s^{-1} motion around the Sun. The CG correction is important because IBEX maps are taken in a way that the same swath of the sky is observed exactly 6 months apart, when IBEX has the opposite orbital velocity around the Sun and therefore needs the opposite CG correction. The methodology for making the CG correction was developed and validated through a consensus process within the IBEX team; the resulting CG correction methodology is described briefly in Appendix A with a more complete development and discussion by R. DeMajistre et al. (Velocity corrected energetic neutral atom spectra from the outer heliosphere, manuscript in preparation, 2010).

[27] Figure 6 compares the first (Figure 6, left) and second (Figure 6, middle) sets of CG-corrected ENA flux maps. Because the maps are corrected to common energies, it is now possible to combine them for improved statistics for studies that are not attempting to examine time evolution. Figure 6, right shows these combined, exposure-time-weighted, averaged maps of ENA flux over an entire year; these maps have reduced statistical errors in some parts of the sky where the sampling times in one or both of the individual maps were extremely limited. An interesting feature revealed in the combined maps is the clear extension of the ribbon toward a complete ring compared to what can be seen in the individual sets of sky maps. These combined maps are available to the broad community, and owing to

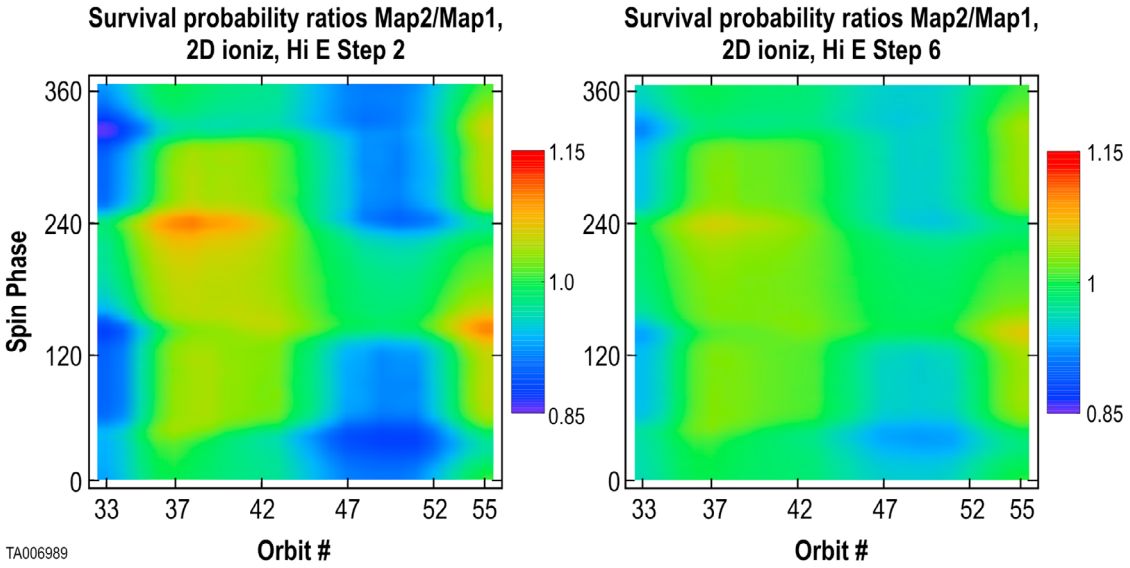

Figure 5. Calculated ratios of the survival probabilities of H ENAs in the second set of sky maps divided by they survival probabilities in the first map for IBEX-Hi energy steps (left) 2 and (right) 6 as a function of spin phase versus orbit number (for Figure 5, right). Ratios for energy steps 3–5 become progressively smaller between these two extremes. Overall, survival probabilities are generally only a few percent different between the two sets of maps, especially at higher energies.

the better coverage and statistics, we recommend them over the individual first and second sets of sky maps for testing hypotheses derived through theory and modeling that are not directly addressing time variations in the ENA flux.

[28] With CG-corrected maps and common color bars shown in Figure 6, it is clear that the gross ENA emissions observed at the ribbon and underlying globally distributed flux are extremely stable over the 6 month interval between the first and second sets of sky maps. In order to better identify and visualize small differences between the two sets of maps, Figure 7 shows equirectangular projected maps of the first (Figure 7, left) and second (Figure 7, middle) sets of IBEX sky maps, highlighting specific intensity levels with red and white outlines as indicated by the red and white arrows on each color bar, respectively. These contours help guide the eye in comparing specific quantitative flux levels. Again, the overall ribbon and general structure appear to be highly similar, although now, some smaller differences are also apparent.

[29] Figure 7, right shows difference maps at each energy, where we have subtracted the flux in each pixel of the first sky maps from the flux in the equivalent pixel of the second sky maps. Red indicates higher ENA fluxes in the second map compared to the first, or increasing flux over the 6 months between observations; similarly, blue indicates decreasing flux over these 6 months. Several artificial features are evident in the regular sky maps and amplified in these difference maps. In particular, the rectangular maps enable identification of vertical stripes that correspond to an apparent enhanced ENA flux throughout the swath acquired over a single orbit. These result from an abnormally high and mostly uniform background present during most of an orbit or an orbit with poor statistics due to removal of time intervals of high background during an orbit. These features are particularly evident over longitude ranges of ~70° to 90° and ~180° to −150°.

[30] Additionally, there is still a discontinuity in fluxes at angles of ~0° and ~180°, where the first (11 and 34) and last (33 and 56) orbits of each map abut each other. This was far more significant in the uncorrected images (Figure 3) compared to the CG-corrected ones (Figure 6) showing that this correction has largely accounted for the differences in flux. However, in the difference maps of Figure 7, one can still see a general redness in the hemisphere between ~0° and ~180° and general blueness in the opposite hemisphere, especially at lower latitudes and in the lower energies. This could represent a real change in the globally distributed ENA flux being observed by IBEX, with increasing ENA emissions from the nose and decreasing emissions from the tail between the two sets of maps. However, because the discontinuity occurs at angles of ~0° and ~180°, this apparent difference is far more likely to be produced by imperfect CG correction of the maps. A small systematic error in the CG correction (e.g., if there is still some residual background noise in the lower-energy channels) will produce slight apparent asymmetries between the ram and antiram viewing directions, especially at lower energies and latitudes.

[31] Notwithstanding the orbits with very low counting statistics and potentially imperfect CG corrections, Figure 7 clearly shows some real differences between IBEX's first and second sets of sky maps. First, both the north and south polar regions have reduced ENA fluxes in the second map compared to the first, as evidenced by the blue across the top and bottom of the difference maps. The effect appears to be a significant reduction in ENA flux over the 6 months between the two maps. Because the magnitude of the CG correction is smaller at the higher energies and decreases

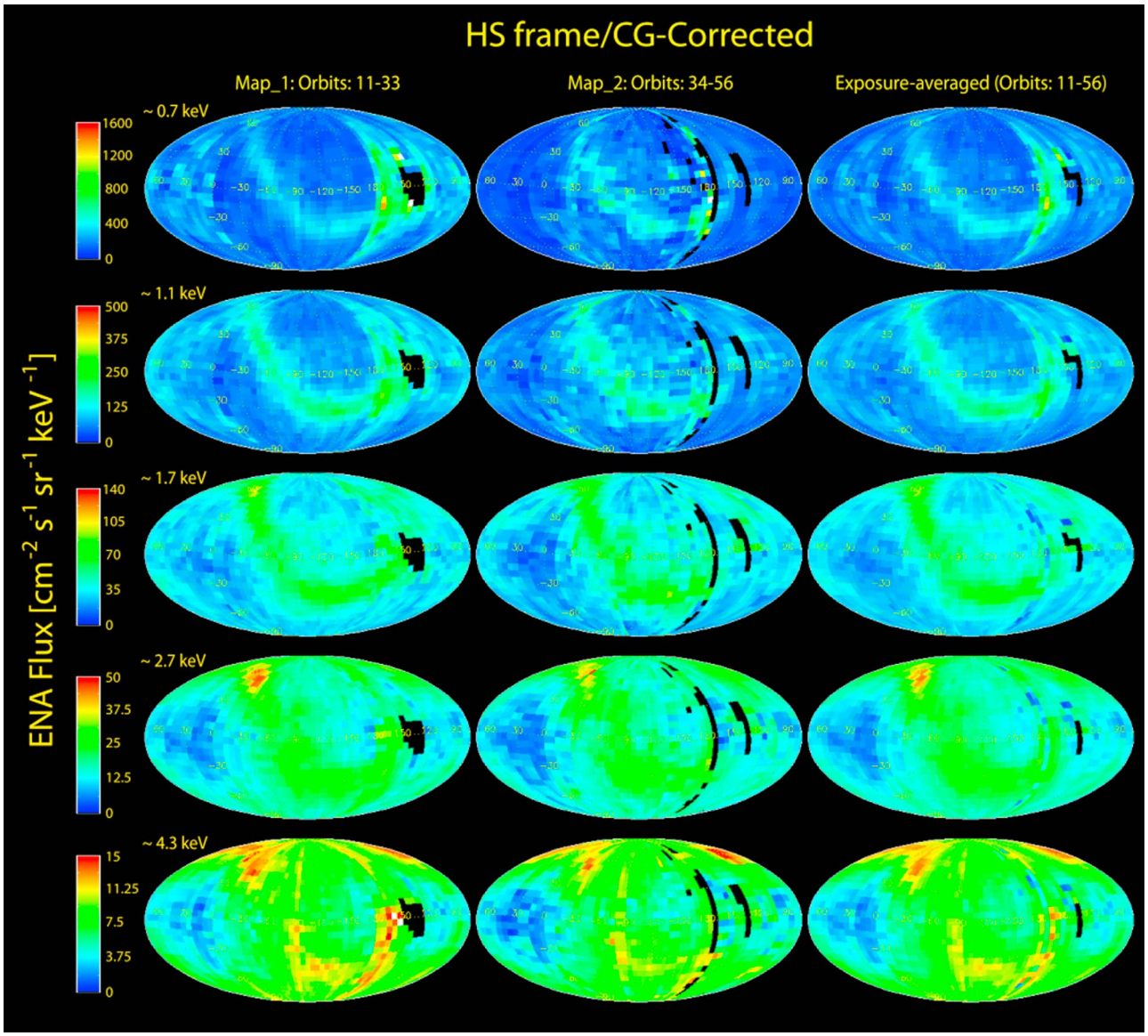

Figure 6. Compton-Getting corrected ENA fluxes for the (left) first, (middle) second, and (right) combined sets of all-sky maps from IBEX. While the second maps are somewhat noisier, the common color bar for each energy range allows for rapid quantitative comparison. The maps clearly show similar structures and fluxes, although some statistically significant differences are observed.

with increasing latitude (becoming zero at the poles), it cannot be responsible for this observed change.

[32] Figure 8 shows a more quantitative analysis of the change in high-latitude flux between the first and second sets of sky maps. Here, we calculated exposure-weighted fluxes and associated uncertainties in 2° latitudinal bands by summing over all azimuths. We then integrated these fluxes and their uncertainties starting at both poles and including increasing numbers of lower latitudinal bands. Thus, for each latitude in Figure 8, the flux and associated uncertainty represent integrations of ENA observations poleward of that latitude and over all longitudes.

[33] The results in Figure 8 are extremely consistent, with both poles showing significantly lower fluxes (Figure 8, left) in the second maps at the various energies separately and for all energies combined. Figure 8, right provides accumulated uncertainties as the integrations extend to lower latitudes. Uncertainties decrease with integration over an increasing range of latitudes down from the poles and reach minima (~25° S and ~15° N from the poles, indicated by yellow regions) prior to growing as the integrations start to include additional lower-latitude structure, such as the ribbon. By using values around the uncertainty minima, this technique provides robust measures of the differences in ENA flux from the two polar regions. Furthermore, the survival probabilities are essentially identical for the polar regions, when integrated over all orbits in the maps (see Figure 5). The overall reduction in flux at both poles is clear and represents

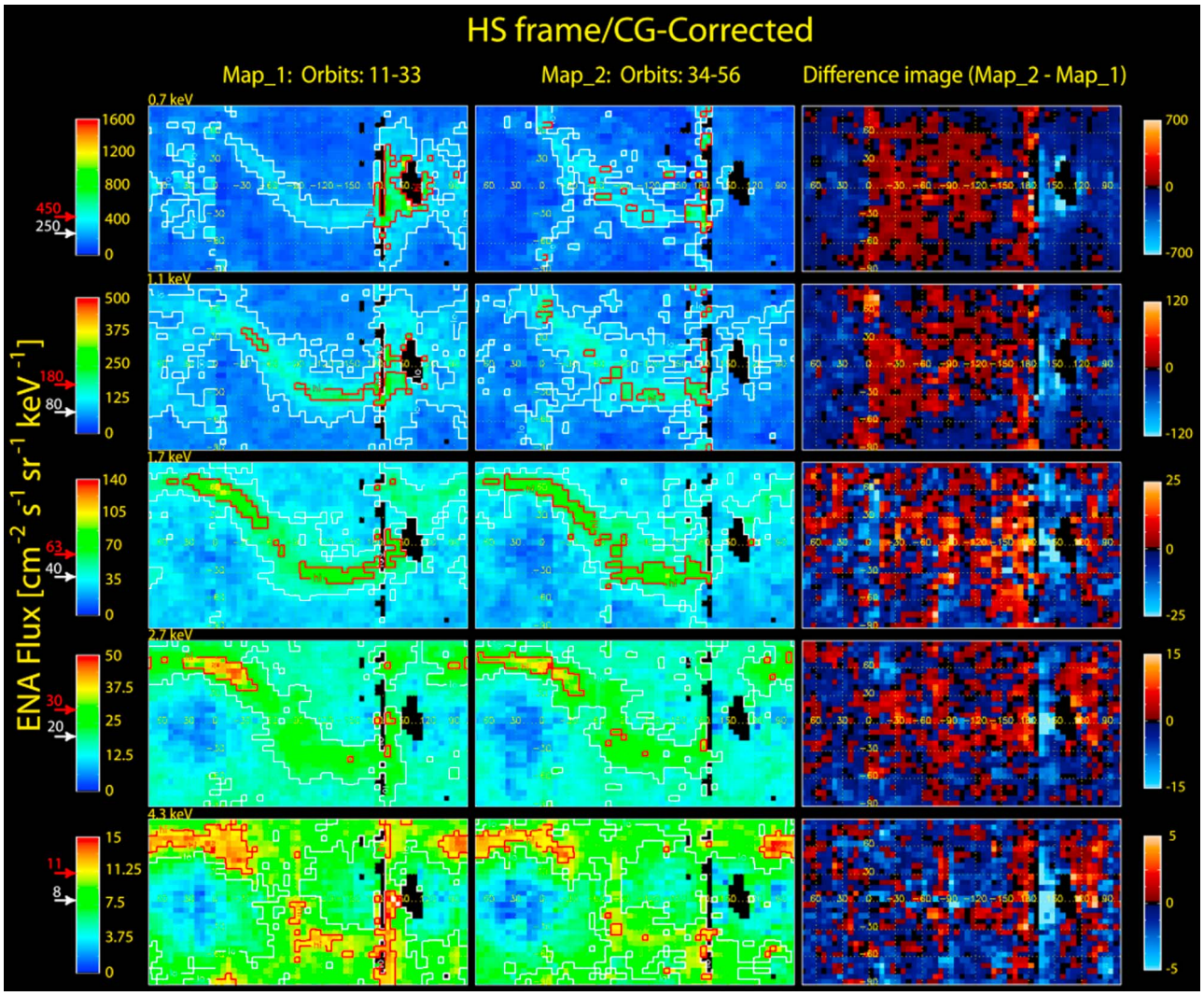

Figure 7. Equirectangular projections of CG-corrected (left) first and (middle) second sets of IBEX all-sky maps with specific contours (red and white outlines with values indicated by arrows next to color bars) to help guide the eye. (right) The difference images where red (blue) indicates more (less) flux in the second map compared to the first.

a decrease of ~10–15% over 6 months across the entire energy range from ~0.5–6 keV.

[34] A second small change that can be seen in the sets of sky maps in Figure 7 are some detailed spatial variations and an apparent northward motion of the southern, nearly horizontal (roughly fixed latitude) portion of the ribbon, between longitudes of ~90°–180°. This shows up both in differences between the locations of the contours in Figures 7, left and 7, middle and in the difference maps as a characteristic combination of a decreased (blue) region immediately southward of an increased (red) region; these two indicators show up to a greater or lesser extent in all five energy channels shown. This apparent motion is only one pixel (~6°), which is the angular resolution of the IBEX sensors. Thus, while consistent differences over a large longitude range and multiple energies are highly suggestive of a real, albeit small, temporal change in the overall ENA emissions, this change cannot be considered definitive.

[35] The third difference between the first two sets of IBEX sky maps, on the other hand, is a clear change in the "knot" region in the northern portion of the IBEX ribbon [*McComas et al.*, 2009b; *Funsten et al.*, 2009a], which exhibits flux enhancements at higher energies in the first sky maps. In the second set of maps, this knot is substantially diminished and appears to spread out both to lower latitudes at the same longitude and to higher latitudes at longitudes away from the nose. Figure 9 magnifies the region of the 2.7 keV maps around the knot. Contours at the same flux levels help guide the eye for changes between the maps and again in the difference image (Figure 9, bottom); blue indicates a reduction and red an enhancement over the 6 months between the maps. Clearly the ENA emissions from the small region of the knot are substantially reduced in the second maps. Additionally, there is some evidence for enhanced emissions in the second maps both poleward along the ribbon (upper left red region in the difference

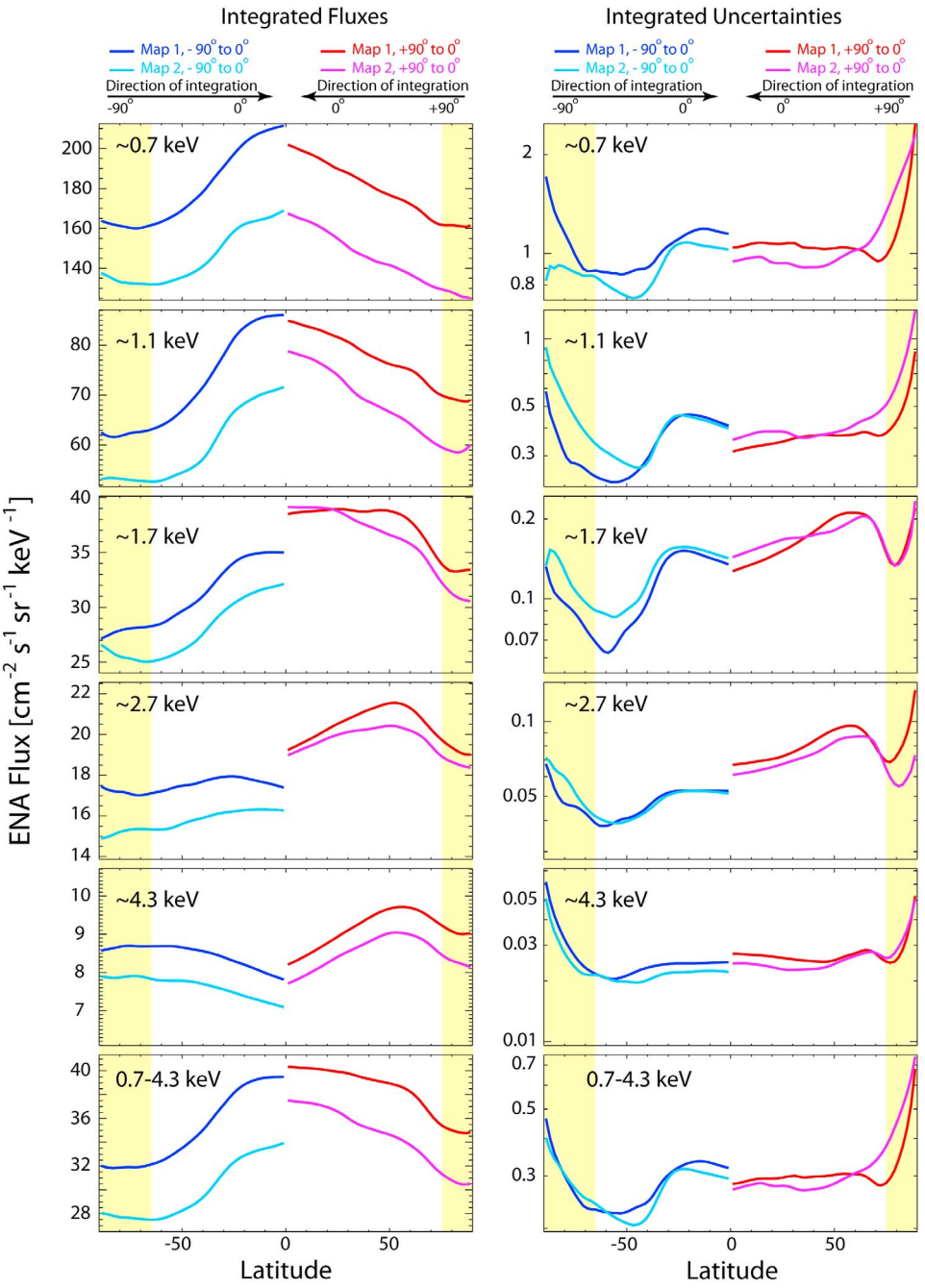

Figure 8. Quantitative comparison of ENA fluxes from the south (blues) and north (reds) between IBEX's first (dark blue and red) and second (light blue and red), sky maps using 2° resolution. (left) The difference in integrated CG-corrected flux for each of the energy steps (and all steps summed – bottom), and (right) the overall uncertainty of the integrated flux (see text). Yellow-shaded regions highlight the polar regions.

image) and southward (lower right red region in the difference image), compared to the first. The overall reduction in the knot emissions are substantial, with roughly one fourth to one third less emission observed over 6 months.

[36] As one final quantitative comparison between the two sets of sky maps, we divided the maps into three contiguous regions as shown in Figure 10: (1) the ribbon region, encapsulated in a shell of width ±18° centered at ecliptic coordinates of 221°, 39° as found by *Funsten et al.* [2009a]; (2) the nose and N pole region outside of the ribbon; and (3) the tail, flanks, and south pole region outside of the ribbon. Table 2 provides the ratio of exposure-weighted averaged fluxes in the second set of CG-corrected all-sky maps compared to the first set (6° × 6° pixels) for each pair of full maps and for these three regions separately. The fluxes are time-exposure-weighted values based on all pixels within

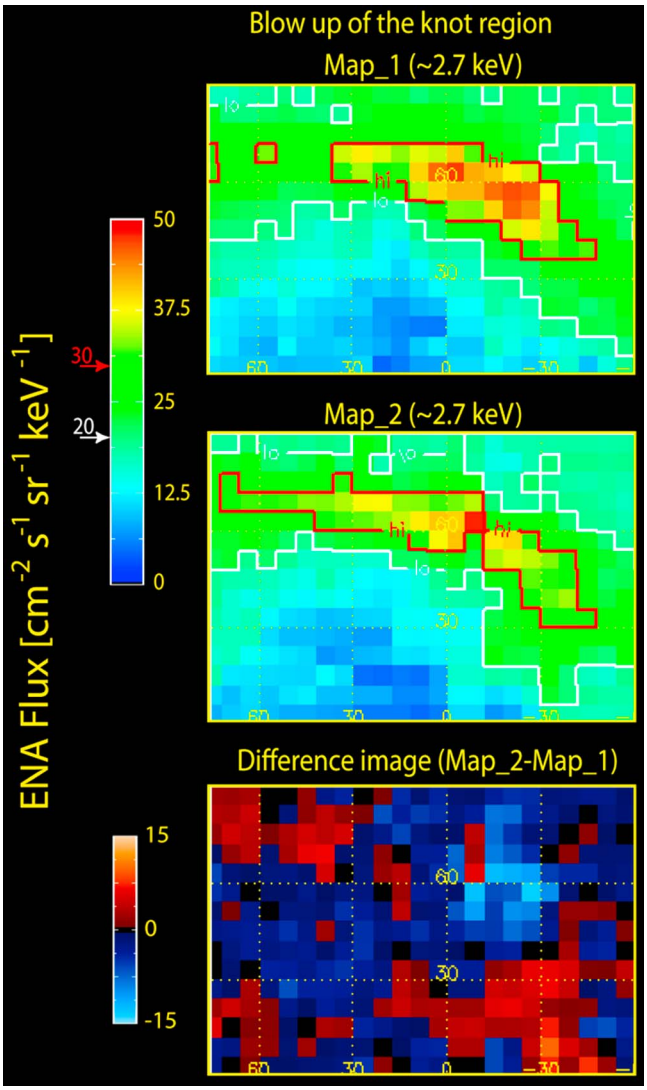

Figure 9. Blow up of the knot region in the northern part of the ribbon in map (top) 1 and (middle) 2 at ~2.7 keV. (bottom) The difference image of this region for all pixels. Clearly, the knot emissions have significantly diminished (and possibly spread out) between the two maps.

each region; errors are calculated from error propagation of the standard deviations of the fluxes. The overall ENA fluxes are reduced in the second set of maps compared to the first. The errors shown, however, do not include nonstatistical errors, such as residual, unsubtracted backgrounds. While small, these backgrounds can have a substantial impact on the lower-energy channels (bold in Table 2), the effects of which are further amplified by the CG-correction process, which is highly sensitive to the energy spectrum. On the other hand, the results in the top two energies (>2 keV) are less effected and indicate small reductions in the ENAs measured by IBEX.

3. Discussion

[37] New observations from IBEX provided in this study show that (1) the globally distributed ENA fluxes from the outer heliosphere are extremely stable over the 6 months between observations in the first two sets of IBEX sky maps and (2) the ribbon of enhanced ENA flux is also extremely stable over the interval between the first two maps. However, some statistically significant differences indicate that the outer heliosphere is noticeably evolving over this short (6 month) timeframe. In particular, (3) the overall ENA emissions observed by IBEX above ~2 keV appear to be slightly lower in the second set of sky maps compared to the first, both within the ribbon and outside of it; (4) both the north and south poles have significantly lower (~10–15%) ENA emissions in the second set of sky maps compared to the first across the energy range from 0.5 to 6 keV; (5) the "knot" in the northern portion of the ribbon in the first maps is less intense and appears to have spread and/or somewhat dissipated by the time the second set of maps was acquired; and (6) the detailed fluxes in the southern (horizontal) portion of the ribbon have evolved and there may be a slight (one pixel, ~6°) equatorward motion of its center.

[38] The fact that both the globally distributed ENA flux and ENA emissions of the bright ribbon are largely stable between IBEX's first two sets of sky maps indicates a largely stable heliospheric interaction and global configuration. It takes roughly 1 year for 1 keV solar wind to reach the TS at ~90 AU and then from 0.5 to nearly 2 years for ENAs in the IBEX-Hi energy passbands to transit back ~100 AU from the inner heliosheath (see Table 3); ENAs coming from the outer heliosheath, two to three times further away take proportionally longer. Given the immense scale of the heliosphere and its interstellar interaction, the many year time scales involved in plasma propagating through this structure, and the anticipated long LOS integration paths producing ENAs in the outer heliosphere, it would in fact have been far more surprising if the overall structure was not largely stable for the short time of observations reported here. In future studies, we plan to use time-lagged observations from various energies to reconstruct the source fluxes in the outer heliosphere at fixed times in the past. Still, even with just the first year of IBEX data, there are clear differences between the first two sets of maps, indicating evolution of both globally distributed, and more localized, ribbon fluxes of ENAs over only 6 months. Such variations likely indicate relatively thin source regions, at least for the portions of the ENA emissions that are varying over this short timescale.

[39] For the globally distributed flux, emissions from both polar regions were reduced by ~10–15% over the 6 months between the first two maps. This reduction might be related to decreasing solar wind flux over the past several years [*McComas et al.*, 2008] that should decrease the density of the inner heliosheath. If these changes are caused by the evolution of the global solar wind through the solar cycle then there may be as much as a factor of two variation in ENA fluxes from the global heliosphere over the ~11 year solar cycle. We note that the observation of polar evolution is a robust result because the CG correction to the data is extremely small at the higher latitudes.

[40] While it is possible that a second, apparent enhancement in the hemisphere toward the nose (and reduction in the opposite hemisphere) could indicate real changes in the globally distributed flux, such as an enhancement (decrease) in heliosheath thickness and/or ion fluxes in nose (tail), we

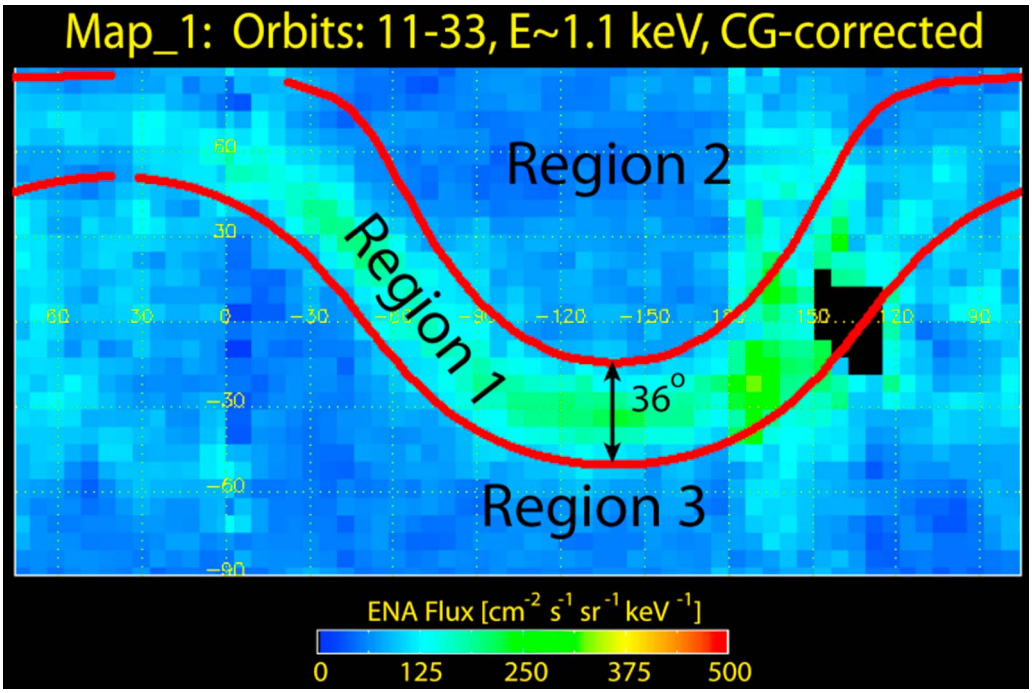

Figure 10. Energy step 3 (1.1 keV) sky map showing the three regions used for Table 2: (1) the ribbon, (2) the nose and N pole region, and (3) the tail, flanks, and S pole region.

think it is far more likely that this apparent difference is actually caused by an imperfect CG correction, which would have the largest effect at the lowest energies and latitudes, as seen in the CG-corrected images.

[41] In the ribbon, there are small but real variations between the maps, and thus time evolution. The southern, horizontal portion of the ribbon appears to move northward (toward the equator) possibly one pixel (6°), which is essentially the resolution of IBEX-Hi. If this is actually a transverse motion of the source for this portion of the ribbon, then for a source at ~100 AU, one pixel (6°) indicates a transverse speed of ~100 km s^{-1}; for a source at ~250 AU, as suggested by the secondary ENA emission model (3), in the outer heliosheath this would indicate a transverse speed of ~250 km s^{-1}. Finally, this apparent equatorward motion is opposite to what would be expected for convection of structures away from the nose either along the heliopause or in the inner or outer heliosheath.

[42] As discussed above, the ribbon occupies a region where the interstellar magnetic field in the outer heliosheath is roughly perpendicular to the LOS [*McComas et al.*, 2009b]; this is the region for which $\mathbf{B} \cdot \mathbf{r} \sim 0$, where **B** is the interstellar magnetic field that is compressed in the outer heliosheath as the interstellar flow deflects around the heliopause [*Schwadron et al.*, 2009]. In fact, the compression of the interstellar flow shifts the location of the ribbon from a great circle (with angular radius of 90°) into an arc with an angular radius of <90° [*Funsten et al.*, 2009a]. We expect that greater compression and deflection of interstellar flow near the nose causes the region of $\mathbf{B} \cdot \mathbf{r} \sim 0$ to decrease in angular radius, therefore causing much of the ribbon to move equatorward, as observed. This opens an important question about the potential for global changes in the properties of the solar wind in the inner heliosheath to affect the deflection of interstellar flow around the heliosphere, and therefore the location of the ribbon. For example, blunting of the TS and heliopause, which may be related to a temporary (several years) reduction in solar wind ram pressure, would lead to greater compression and deflection

Table 2. Ratios of ENA Fluxes in Second Maps Compared to First Maps[a]

	Ratio of Weighted Fluxes (F_{Map_2}/F_{Map_1})			
Energy (keV)	Ribbon (1 in Figure 10)	Nose/N Pole (2 in Figure 10)	Tail/Flanks/S Pole (3 in Figure 10)	All Sky
~0.7	**0.89 ± 0.03**	**0.95 ± 0.03**	**0.67 ± 0.01**	**0.79 ± 0.01**
~1.1	**0.90 ± 0.02**	**0.99 ± 0.02**	**0.79 ± 0.01**	**0.87 ± 0.01**
~1.7	0.98 ± 0.02	1.02 ± 0.02	0.92 ± 0.01	0.98 ± 0.01
~2.7	0.96 ± 0.01	0.98 ± 0.01	0.96 ± 0.01	0.97 ± 0.01
~4.3	0.91 ± 0.01	0.92 ± 0.01	0.92 ± 0.01	0.92 ± 0.01

[a]Systematic errors make bold results less reliable.

Table 3. The100 AU Transit Times for ENAs in IBEX-Hi Energy Passbands

E Step	E_{-FW} (days)	E_{-FWHM} (days)	$E_{Nominal}$ (days)	E_{+FWHM} (days)	E_{+FW} (days)
2	668	580	469	405	356
3	519	431	380	317	284
4	382	339	290	250	227
5	305	280	240	204	185
6	247	223	195	161	150

of interstellar flow around the heliopause and, possibly, equatorward motion of the region where $\mathbf{B} \cdot \mathbf{r} \sim 0$.

[43] The portion of the ribbon that shows clear time variation between the first two maps is the knot in its northern region. Clearly, the brightest emissions at high energies in the first set of sky maps are significantly diminished and spread out toward both higher and lower latitudes; while the apparent spread northward and away from nose could be consistent with convection away from nose, the southward enhancement is not. Evolution of the knot indicates a spectral change, in which the flux in the central area of the knot has become more like the adjacent sections of the ribbon and less like the most polar regions, which all showed enhancements at the higher IBEX energies [*Funsten et al.*, 2009a]. It is interesting to consider if this change could be associated with the boundary between the fast and slow solar wind regions moving and slower solar wind populating the inner heliosheath at the latitude of the knot.

[44] Given the largely stable structure, but clear evidence for evolution of at least some portions of the ribbon, it is important to ask what the implications are for various competing ideas about the source of the ribbon. Here we comment on each of the six mechanisms suggested by *McComas et al.* [2009b] and discussed above.

3.1. Maximum Pressure and Stagnation (1 in Figure 1)

[45] In this explanation, the primary ribbon location should be generally stable owing to the large-scale external pressure driver; however, changing internal pressure, for example from small changes in the solar wind over time, could produce small changes in observed ENA fluxes. Also, fine structure could be variable if produced by extrusions, which are instabilities on the heliopause. Overall, based largely on the ribbon's general stability, this explanation appears consistent with the observations.

3.2. Primary ENAs From Compressions (2 in Figure 1)

[46] This concept is similar to maximum pressure and stagnation in that the large-scale structure would be expected to be largely stable since it comes from the external pressure, but fine structure should vary since it is mostly driven by small-scale compressional instabilities in the draped LISM field, most likely close to the heliopause. In this case, the ribbon would likely be less sensitive to solar wind changes than maximum pressure and stagnation, since the ENA production occurs in the outer heliosheath instead of the inner heliosheath. However, the fact that the population is highly suprathermal indicates that it may be produced, at least partially, by secondary ENAs (3 in Figure 1), in which case the population would be sensitive to changes in the solar wind.

3.3. Secondary ENAs (3 in Figure 1)

[47] The mechanism is related to primary ENAs from compression, but solar wind and inner heliosheath ENAs produce ions that become reneutralized, so solar wind changes are probably more visible. Also, this process should occur continuously over large distances along the LOS (ionization lengths: ~550 AU beyond the heliopause at 1 keV and ~900 AU at 5 keV owing to scale lengths of ionization via charge exchange assuming a 0.07 cm^{-3} LISM proton density). With the need to accumulate emission over a length >550 to 900 AU, this model has trouble producing significant variations over times as short as 6 months. For example, at 1 keV a secondary ENA takes ~6 years to transit the 550 AU ionization length, and therefore >12 years to move from the solar wind into the LISM, and then back into the heliosphere where it can be detected. Finally, this mechanism doesn't produce fine structure unless combined with primary ENAs from compression, in which case it could be variable.

[48] If the ribbon is formed outside the heliopause, then its location will shift with temporal variations in ENA energies. The locus of sightlines that are perpendicular to the interstellar magnetic field lines, $\mathbf{B} \cdot \mathbf{r} = 0$, varies with distance beyond the heliopause as field lines bend around the heliosphere. The energy-dependent mean-free paths of ENAs therefore should affect the location of the ribbon's arc. The finite widths of the IBEX-Hi energy channels (Table 1) translate into a range of mean-free paths represented by the fluxes in a single channel (Table 2). For instance, the ionization length of ENAs in energy step 3 range from 490 AU to 570 AU in a 0.074/cc density plasma as appropriate for the outer heliosheath. The nearly horizontal portion of the ribbon shifts northward by approximately 0.7 degrees per 10 AU decrease in the mean-free path of an energy step 3 ENA, according to the heliosphere model of *Schwadron et al.* [2009], so this path difference due to the channel width adds about six degrees to the ribbon width. This sensitivity of the ribbon location to variations in the energy of the parent ion suggests that comparisons between small shifts in the ribbon location and the time-lagged solar wind properties may provide clues to the origin region of the ribbon.

3.4. ENAs From Magnetic Reconnection at the Heliopause (4 in Figure 1)

[49] If the LISM field is stable over the times examined here and the solar wind's interplanetary magnetic field paints the heliopause surface with alternating bands that are only one solar rotation (26 days) wide [*Suess*, 2004], then the structure might be expected to be narrowly banded (nonrandom) and moving away from the nose. Generally speaking, the appearance of the ~20° wide ribbon instead of numerous, distributed source regions across the heliopause may seem inconsistent with this explanation, although, if the reconnection was strongly organized by the pressure maximum pushing the external and internal magnetic field together at the heliopause, this might generate such a structure. Reconnection could produce time-variable patches within the ribbon.

3.5. ENAs From Shock-Accelerated Pickup Ions (5 in Figure 1)

[50] A maximum pressure region could push in the TS locally to somehow trigger localized production of pickup ions and subsequently enhanced ENA production. Since the TS moves in and out and varies with the solar wind properties, this mechanism might be expected to be the most variable over the solar cycle.

3.6. ENAs From Heliopause Instabilities (6 in Figure 1)

[51] This process should produce structures that always move away from the nose (assuming it is the highest pressure region). For transverse speeds of ~100 km s^{-1}, this would give ~6° (one pixel) per 6 months. This is about the rate of the possible motion of the southern portion of the ribbon; however, if that portion of the ribbon did move, it appeared to move toward the nose and not away from it, as the mechanism would suggest. Finally, this process could produce fine-scale structures, which would vary over time, but it would likely move away from the nose also.

[52] For the seventh mechanism suggested by *Grzedzielski et al.* [2010], any variations on such short timescales seem problematic for ENAs produced by charge exchange between neutral H atoms at the nearby edge of the LIC and hot protons from the Local Bubble owing to the immense scale of this interaction. On the other hand, even if this mechanism is operating, the ENA flux observed by IBEX likely derives from a combination of sources including a more "local" heliospheric one, which could account for observed temporal variations.

[53] The IBEX mission continues to provide a wealth of new information about the outer heliosphere and its interaction with the LISM. This overall interaction appears to be evolving over time, most likely as the solar wind evolves over the solar cycle. Observations from IBEX are continuing and each roughly weeklong orbit returns another swath of the sky, building up new sets of sky maps each 6 months. While the mission was designed and originally slated to last only 2 years, the IBEX team used some of the spacecraft's remaining hydrazine after launch to quickly raise the orbit perigee and reduce the radiation fluence from passing through the Earth's radiation belts. Thus, with a little luck, IBEX will continue its remarkable mission of discovery and exploration for many years to come, allowing us to sample the outer heliospheric ENAs over the solar cycle.

Appendix A: Compton-Getting Correction of the Data

[54] The IBEX spacecraft moves around the Sun with a velocity that is a measurable fraction of the velocity of the ENAs being measured. Therefore, a Compton-Getting correction is needed to quantitatively compare measurements taken at different parts of the year. The first two 6 month maps are transformed from the spacecraft reference frame into the inertial reference frame at the central energy of each of the highest five instrument energy steps (0.71, 1.11, 1.74, 2.73, and 4.29 keV). The Earth's orbital velocity is ~30 km s^{-1}, which is nearly 7% of the velocity of a 1 keV H atom (the orbital velocity of IBEX around the Earth is ~1 km s^{-1} and will be neglected here). Figure A1 shows the change in angle and energy for the transformation of an ENA from a fixed energy in the spacecraft frame to the inertial reference frame. The change in angle and energy depend on the central look direction of the sensor as it rotates about the spin axis directed approximately toward the Sun. In general, the effects associated with the change in reference frame become most important at the lowest energy steps observed by IBEX, and the corrections are relatively small (<5° change in angle, and <15% change in energy) at the energies analyzed here (>0.7 keV).

[55] The reference frame changes in energy and angle are particularly important when comparing sky maps obtained 6 months apart, since each map is derived from opposite halves of the year, and thus opposing orbital velocity directions. For example, in Figure 2 we see that the nose of the heliosphere is imaged in March. Since the orbital velocity and actual velocity of the particle are added in the observation, the apparent velocity of the ENAs from the nose direction is larger in the IBEX spacecraft's frame of reference. That is, IBEX will effectively sample lower-energy heliospheric ENAs from the nose. Six months later, in September, the nose is again imaged, but this time in the wake direction (opposed to the velocity vector), so IBEX effectively samples higher-energy heliospheric ENAs at the same energy step. In order to compare maps taken 6 months apart we must correct for the difference in effective sampling energy in the two maps. This appendix describes the correction implemented in the IBEX data analysis. It is worth noting that this particular correction methodology was vetted through a consensus process with the IBEX science team, which included significant testing and validation.

[56] Let $\mathbf{v}$ be the velocity vector of an ENA in the IBEX frame (Figure A2). The IBEX spacecraft moves with the velocity $\mathbf{u}_{SC}$ with respect to the solar inertial frame. The velocity vector of the ENA in the solar inertial frame, $\mathbf{v_i}$, is therefore $\mathbf{v_i} = \mathbf{v} + \mathbf{u_{SC}}$. IBEX measures ENAs in a plane nearly perpendicular to the direction of the Sun, and the ENA incidence velocity angle, θ, is the incoming velocity angle of the ENA referenced to Ecliptic North in right-handed rotation about the sunward axis (Z). Note that the incidence velocity angle, θ, represents the angle between the vector, $-\mathbf{v}$, and the North Ecliptic Pole (NEP). We represent vectors in a coordinate system where the x axis points toward the NEP, the y axis points in the direction of Earth's motion about the Sun (these are Z_{GSE} and $-Y_{GSE}$), and the Z axis is directed toward the Sun. With this representation, Galilean transformations are explicitly

$$v\begin{vmatrix}\cos\theta\\ \sin\theta\end{vmatrix} = v_i\begin{vmatrix}\cos\theta_i\\ \sin\theta_i\end{vmatrix} + \begin{vmatrix}0\\ u_{SC}\end{vmatrix}. \tag{A1}$$

The magnitude of the velocity in the inertial frame is therefore

$$v_i = v\sqrt{1 - 2\left(\frac{u_{SC}}{v}\right)\sin\theta + \left(\frac{u_{SC}}{v}\right)^2} \tag{A2}$$

the angular aberration between the systems is

$$\begin{aligned}\cos\theta_i &= \frac{v}{v_i}\cos\theta\\ \sin\theta_i &= \frac{v}{v_i}\sin\theta - \frac{u_{SC}}{v_i}\end{aligned} \tag{A3}$$

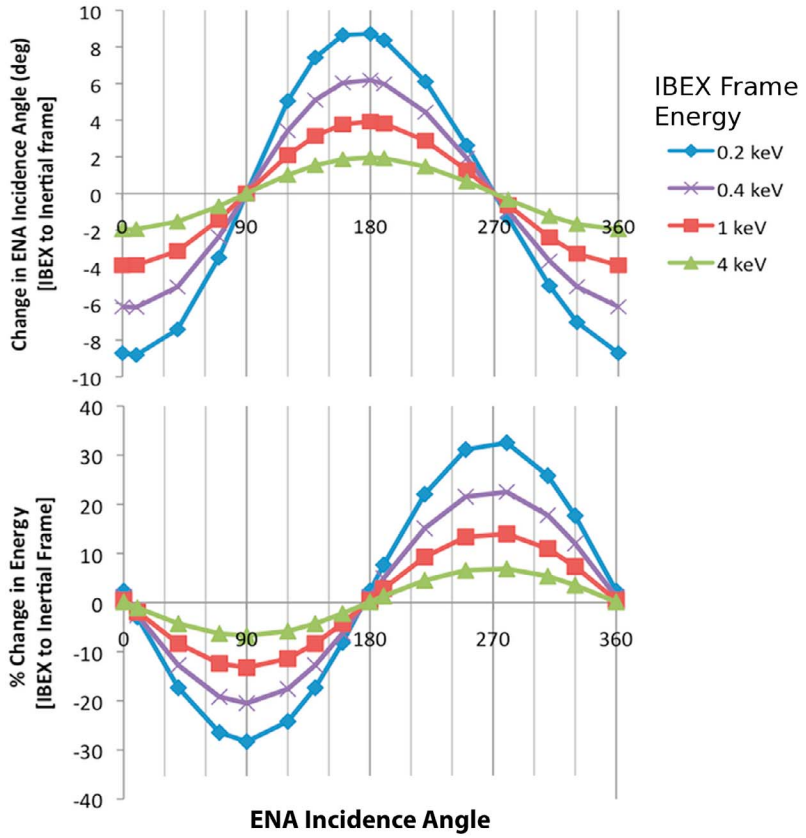

Figure A1. The change in (top) ENA incidence angle and (bottom) energy from the IBEX reference frame to the inertial frame as a function of the ENA incidence angle measured from the North Ecliptic Pole in the spacecraft frame. The spacecraft rotates about the spin axis directed approximately toward the Sun, with each of the sensors directed approximately perpendicular to the spin axis. A sensor measures an ENA incidence angle of 0° where the sensor bore sight points to the NEP (see Figure A2). Since the spacecraft spins in a right-handed sense, an ENA incidence angle of 90° is measured where the sensor bore sight is directed roughly along the vector of Earth's motion about the Sun. An ENA incidence angle of 180° is measured where the bore sight is directed along the South Ecliptic Pole, and an incidence angle of 270° is measured where the bore sight is directed opposite to Earth's motion.

and the ratio of the energies is

$$\frac{E_i}{E} = \frac{\mathbf{v}_i \bullet \mathbf{v}_i}{\mathbf{v} \bullet \mathbf{v}} = 1 - 2\frac{u_{SC}}{v}\sin\theta + \left(\frac{u_{SC}}{v}\right)^2. \tag{A4}$$

The invariance of phase-space density requires that the ENA flux in the solar inertial frame, $j_i(\theta_i, E_i)$, be related to the ENA flux in the IBEX spacecraft frame, $j(\theta, E)$, as

$$j_i(\theta_i, E_i) = \frac{E_i}{E} j(\theta, E), \tag{A5}$$

which along with the equations above, allows us to express the ENA flux in the solar inertial frame given measured fluxes in the IBEX frame. It is important to note, however, that for measurements at a fixed energy and a regular angle grid, the resulting fluxes in the solar inertial frame will be given at multiple energies on an irregular angular grid. This is rather awkward for producing maps and makes comparison of maps taken 6 months apart difficult. We therefore develop a method that allows us to produce estimates of the flux in the solar inertial frame at fixed energies and on a regular angle grid.

[57] Fluxes at a fixed energy in the solar inertial frame will require us to estimate fluxes in the IBEX frame at various energies. Given a spectrum of measured fluxes at the nominal IBEX channel energies, $j_n = j(\theta, E_n)$, we can estimate the flux at nearby energies using the log-log Taylor expansion from

$$\ln j_{est}(\theta, E) = \ln j_n + k_n \ln\frac{E}{E_n} + \frac{a_n}{2}\left(\ln\frac{E}{E_n}\right)^2 + O\left[\left(\ln\frac{E}{E_n}\right)^3\right], \tag{A6}$$

where the derivatives of the spectrum

$$k_n = \left.\frac{\partial \ln j}{\partial \ln E}\right|_{E_n}, a_n = \left.\frac{\partial^2 \ln j}{\partial (\ln E)^2}\right|_{E_n} \tag{A7}$$

are determined numerically from the measured spectrum. For convenience, we calculate the fluxes in the solar inertial

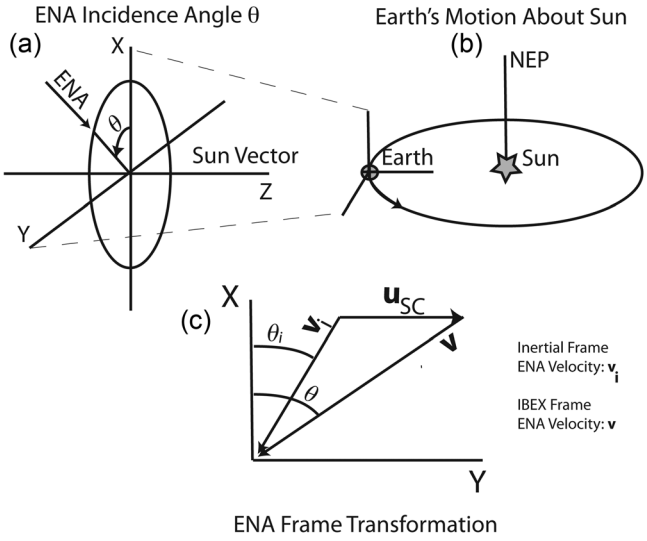

Figure A2. The motion of Earth about the Sun makes it necessary to transform ENA measurements from the IBEX reference frame to an inertial reference frame fixed with the Sun. The geometry of this frame transformation is illustrated here. The IBEX spacecraft has an approximately Sun-pointed spin axis, and we measure incident ENAs in the spin plane roughly perpendicular to the spin axis. (a) The incident ENA velocity angle, θ, is measured relative to the NEP (x axis) in the spin plane as a right-handed rotation about the Z axis. (b) The y axis is directed along the vector of Earth's motion around the Sun. (c) In the spin plane, the inertial frame ENA velocity, $\mathbf{v}_i$, is the sum of the spacecraft velocity, $\mathbf{u}_{SC}$, and the measured ENA velocity, $\mathbf{v}$.

frame at the nominal channel energies, E_n, and therefore write

$$j_i(\theta_i, E_n) = \frac{E_n}{E} j_{est}(\theta, E), \tag{A8}$$

where the variable energy, E, is determined by the ratios of the energies written above (A4).

[58] In practice, we first calculate the required energy in the IBEX frame using (A4), then determine the fluxes in the solar inertial frame using (A6) and (A8). Note that (A8) is given on the irregular angular grid, θ_i. We then use a simple linear interpolation to regrid these results back to the measurement grid, θ. We have therefore transformed measurements of fluxes in the IBEX measurement frame into the solar inertial frame at fixed energies on a regular angle grid, the results of which allow us to compare maps taken 6 months apart. A more complete development and discussion of how we correct for the CG effect in IBEX data are given by DeMajistre et al. (manuscript in preparation, 2010).

[59] **Acknowledgments.** We thank E. C. Roelof for work on the CG effect and are deeply indebted to all of the outstanding men and women who have made the IBEX mission such a wonderful success. This work was carried out as a part of the IBEX project, with support from NASA's Explorer Program and Polish Ministry for Science and Higher Education grant NS-1260-11-09.

[60] Philippa Browning thanks the reviewers for their assistance in evaluating this manuscript.

References

Auchère, F., J. W. Cook, J. S. Newmark, D. R. McMullin, R. von Steiger, and M. Witte (2005), The heliospheric He II 30.4 nm solar flux during cycle 23, *Astrophys. J.*, *625*(2), 1036–1044, doi:10.1086/429869.

Borovikov, S. N., N. V. Pogorelov, G. P. Zank, and I. A. Kryukov (2008), Consequences of the heliopause instability caused by charge exchange, *Astrophys. J.*, *682*(2), 1404–1415, doi:10.1086/589634.

Burlaga, L. F., N. F. Ness, and M. H. Acuna (2006), Multiscale structure of magnetic fields in the heliosheath, *J. Geophys. Res.*, *111*, A09112, doi:10.1029/2006JA011850.

Bzowski, M. (2008), Survival probability and energy modification of hydrogen energetic neutral atoms on their way from the termination shock to Earth orbit, *Astron. Astrophys.*, *488*, 1057–1068, doi:10.1051/0004-6361:200809393.

Bzowski, M., T. Mäkinen, E. Kyrölä, T. Summanen, and E. Quémerais (2003), Latitudinal structure and north-south asymmetry of the solar wind from Lyman-alpha remote sensing by SWAN, *Astron. Astrophys.*, *408*, 1165–1177, doi:10.1051/0004-6361:20031022.

Bzowski, M., E. Moebius, S. Tarnopolski, V. Izmodenov, and G. Gloeckler (2008), Density of neutral interstellar hydrogen at the termination shock from Ulysses pickup ion observations, *Astron. Astrophys.*, *491*, 7–19.

Chalov, S. V., and H. J. Fahr (1996), A three-fluid model of the solar wind termination shock including a continuous production of anomalous cosmic rays, *Astron. Astrophys.*, *311*, 317–328.

Chalov, S. V., D. B. Alexashov, D. McComas, V. V. Izmodenov, Y. G. Malama, and N. Schwadron (2010), Scatter-free pickup ions beyond the heliopause as a model for the Interstellar Boundary Explorer (IBEX) ribbon, *Astrophys. J.*, *716*(2), L99–L102.

Fahr, H.-J., I. V. Chashei, and D. Verscharen (2009), Injection to the pick-up ion regime from high energies and induced ion power-laws, *Astron. Astrophys.*, *505*, 329–337, doi:10.1051/0004-6361/200810755.

Funsten, H. O., et al. (2009a), Structures and spectral variations of the outer heliosphere in IBEX energetic neutral atom maps, *Science*, *326*(5955), 964–966, doi:10.1126/science.1180927.

Funsten, H. O., et al. (2009b), The Interstellar Boundary Explorer High Energy (IBEX-Hi) neutral atom imager, *Space Sci. Rev.*, *146*, 75–103, doi:10.1007/s11214-009-9504-y.

Fuselier, S. A., et al. (2009), Width and variation of the ENA flux ribbon observed by the Interstellar Boundary Explorer, *Science*, *326*(5955), 962–964, doi:10.1126/science.1180981.

Grzedzielski, S., M. Bzowski, A. Czechowski, H. O. Funsten, D. J. McComas, and N. A. Schwadron (2010), A possible generation mechanism for the IBEX ribbon from outside the heliosphere, *Astrophys. J.*, *715*(2), L84–L87.

Gurnett, D. A., W. S. Kurth, I. H. Cairns, and J. Mitchell (2006), The local interstellar magnetic field direction from direction-finding measurements of heliospheric 2–3 kHz radio emissions, *AIP Conf. Proc.*, *858*, 129–134, doi:10.1063/1.2359317.

Heerikhuisen, J., N. V. Pogorelov, G. P. Zank, G. B. Crew, P. C. Frisch, H. O. Funsten, P. H. Janzen, D. J. McComas, D. B. Reisenfeld, and N. A. Schwadron (2010), Pick-up ions in the outer heliosheath: A possible mechanism for the Interstellar Boundary Explorer ribbon, *Astrophys. J.*, *708*(2), L126–L130, doi:10.1088/2041-8205/708/2/L126.

Izmodenov, V. V., Y. G. Malama, M. S. Ruderman, S. V. Chalov, D. B. Alexashov, O. A. Katushkina, and E. A. Provornikova (2009), Kinetic-gasdynamic modeling of the heliospheric interface, *Space Sci. Rev.*, *146*, 329–351, doi:10.1007/s11214-009-9528-3.

King, J. H., and N. E. Papitashvili (2005), Solar wind spatial scales in and comparisons of hourly Wind and ACE plasma and magnetic field data, *J. Geophys. Res.*, *110*, A02104, doi:10.1029/2004JA010649.

Krimigis, S. M., D. G. Mitchell, E. C. Roelof, K. C. Hsieh, and D. J. McComas (2009), Imaging the interaction of the heliosphere with the interstellar medium from Saturn with Cassini, *Science*, *326*(5955), 971–973, doi:10.1126/science.1181079.

Lallement, R., E. Quémerais, J. L. Bertaux, S. Ferron, D. Koutroumpa, and R. Pellinen (2005), Deflection of the interstellar neutral hydrogen flow across the heliospheric interface, *Science*, *307*(5714), 1447–1449, doi:10.1126/science.1107953.

McComas, D. J., R. W. Ebert, H. A. Elliott, B. E. Goldstein, J. T. Gosling, N. A. Schwadron, and R. M. Skoug (2008), Weaker solar wind from the polar coronal holes and the whole sun, *Geophys. Res. Lett.*, *35*, L18103, doi:10.1029/2008GL034896.

McComas, D. J., et al. (2009a), IBEX–Interstellar Boundary Explorer, *Space Sci. Rev.*, *146*, 11–33, doi:10.1007/s11214-009-9499-4.

McComas, D. J., et al. (2009b), Global observations of the interstellar interaction from the Interstellar Boundary Explorer (IBEX), *Science*, *326*(5955), 959–962, doi:10.1126/science.1180906.

Möbius, E., et al. (2009), Direct observations of interstellar H, He, and O by the Interstellar Boundary Explorer, *Science*, *326*(5955), 969–971, doi:10.1126/science.1180971.

Pogorelov, N. V., J. Heerikhuisen, J. J. Mitchell, I. H. Cairns, and G. P. Zank (2009), Heliospheric asymmetries and 2–3 kHz radio emission under strong interstellar magnetic field conditions, *Astrophys. J.*, *695* (1), L31–L34, doi:10.1088/0004-637X/695/1/L31.

Prested, C., et al. (2008), Implications of solar wind suprathermal tails for IBEX ENA images of the heliosheath, *J. Geophys. Res.*, *113*, A06102, doi:10.1029/2007JA012758.

Richardson, J. D., J. C. Kasper, C. Wang, J. W. Belcher, and A. J. Lazarus (2008), Cool heliosheath plasma and deceleration of the upstream solar wind at the termination shock, *Nature*, *454*(7200), 63–66, doi:10.1038/nature07024.

Richardson, J. D., E. C. Stone, J. C. Kasper, J. W. Belcher, and R. B. Decker (2009), Plasma flows in the heliosheath, *Geophys. Res. Lett.*, *36*, L10102, doi:10.1029/2009GL038421.

Schwadron, N. A., et al. (2009), Comparison of Interstellar Boundary Explorer observations with 3D global heliospheric models, *Science*, *326*(5955), 966–968, doi:10.1126/science.1180986.

Slavin, J. D., and P. C. Frisch (2008), The boundary conditions of the heliosphere: Photoionization models constrained by interstellar and in situ data, *Astron. Astrophys.*, *491*, 53–68, doi:10.1051/0004-6361:20078101.

Stone, E. C., A. C. Cummings, F. B. McDonald, B. C. Heikkila, N. Lal, and W. R. Webber (2008), An asymmetric solar wind termination shock, *Nature*, *454*(7200), 71–74, doi:10.1038/nature07022.

Suess, S. T. (2004), The magnetic field in the outer heliosphere, *AIP Conf. Proc.*, *719*, 10–15, doi:10.1063/1.1809492.

Tarnopolski, S., and M. Bzowski (2009), Neutral interstellar hydrogen in the inner heliosphere under the influence of wavelength-dependent solar radiation pressure, *Astron. Astrophys.*, *493*, 207–216, doi:10.1051/0004-6361:20077058.

Tobiska, W. K., T. Woods, F. Eparvier, R. Viereck, L. Floyd, D. Bouwer, G. Rottman, and O. R. White (2000), The SOLAR2000 empirical solar irradiance model and forecast tool, *J. Atmos. Sol. Terr. Phys.*, *62*(14), 1233–1250, doi:10.1016/S1364-6826(00)00070-5.

Woods, T. N., F. G. Eparvier, S. M. Bailey, P. C. Chamberlin, J. Lan, G. J. Rottman, S. C. Solomon, W. K. Tobiska, and D. L. Woodraska (2005), Solar EUV Experiment (SEE): Mission overview and first results, *J. Geophys. Res.*, *110*, A01312, doi:10.1029/2004JA010765.

Zank, G. P., H. L. Pauls, I. H. Cairns, and G. M. Webb (1996), Interstellar pickup ions and quasi-perpendicular shocks: Implications for the termination shock and interplanetary shocks, *J. Geophys. Res.*, *101*, 457–477, doi:10.1029/95JA02860.

Zank, G. P., J. Heerikhuisen, N. V. Pogorelov, R. Burrows, and D. McComas (2010), Microstructure of the heliospheric termination shock: Implications for energetic neutral atom observations, *Astrophys. J.*, *708*(2), 1092–1106, doi:10.1088/0004-637X/708/2/1092.

M. Bzowski and M. A. Kubiak, Space Research Centre, Polish Academy of Sciences, Ul. Bartycka 18A, 00-716 Warsaw, Poland.

G. B. Crew, Kavli Institute for Astrophysics and Space Research, Massachusetts Institute of Technology, 77 Massachusetts Ave., Mail Stop 37-515, Cambridge, MA 02139, USA.

M. A. Dayeh, G. Livadiotis, and D. J. McComas, Southwest Research Institute, 6220 Culebra Rd., P.O. Drawer 28510, San Antonio, TX 78228-0510, USA. (dmccomas@swri.org)

R. DeMajistre, Applied Physics Laboratory, Johns Hopkins University, 11100 Johns Hopkins Rd., Laurel, MD 20723, USA.

P. Frisch, Department of Astronomy and Astrophysics, University of Chicago, 5640 S. Ellis Ave., Chicago, IL 60637, USA.

H. O. Funsten, Los Alamos National Laboratory, Los Alamos, Bikini Atoll Road, SM 30, NM 87545, USA.

S. A. Fuselier, Lockheed Martin Advanced Technology Center, 3251 Hanover St., Palo Alto, CA 94304, USA.

M. Gruntman, Division of Astronautical Engineering, Viterbi School of Engineering, University of Southern California, RRB 224, MC-1192, Los Angeles, CA 90089, USA.

P. Janzen and D. B. Reisenfeld, Department of Physics and Astronomy, University of Montana, 32 Campus Dr., Missoula, MT 59812, USA.

E. Möbius and N. A. Schwadron, Space Science Center, University of New Hampshire, Morse Hall, Durham, NH 03824, USA.